



**Diagnosis of Immunomarkers in vivo via Multiplexed
Surface Enhanced Raman Spectroscopy with Gold Nanostars**

Journal:	<i>Nanoscale</i>
Manuscript ID	NR-ART-02-2018-001478.R1
Article Type:	Paper
Date Submitted by the Author:	31-May-2018
Complete List of Authors:	<p>Ou, Yu-Chuan; Vanderbilt University, Chemical and Biomolecular Engineering Webb, Joseph; Vanderbilt University O'Brien, Christine; Vanderbilt University, Biomedical Engineering Pence, Isaac; Vanderbilt University, Biomedical Engineering Lin, Eugene; Vanderbilt University, Radiology and Radiological Sciences Paul, Eden; Vanderbilt University, Chemical and Biomolecular Engineering Cole, Danielle; Vanderbilt University, Chemical and Biomolecular Engineering Ou, Shih-Hao ; Johns Hopkins University Lapierre-Landry, Maryse ; Vanderbilt University, Biomedical Engineering DeLapp, Rossane; Vanderbilt University, Civil and Environmental Engineering Lippmann, Ethan; Vanderbilt University, Chemical and Biomolecular Engineering Mahadevan-Jansen, Anita; Vanderbilt University, Department of Biomedical Engineering Bardhan, Rizia; Vanderbilt University, Chemical and Biomolecular Engineering</p>

Diagnosis of Immunomarkers *in vivo* via Multiplexed Surface Enhanced Raman Spectroscopy with Gold Nanostars[†]

Yu-Chuan Ou,^a Joseph A. Webb,^a Christine M. O'Brien,^{b,c} Isaac J. Pence,^{b,c} Eugene C. Lin,^{d,e} Eden Paul,^a Danielle Cole,^a Shih-Hao Ou,^a Maryse Lapierre-Landry,^{b,c} Rossane C. DeLapp,^f Ethan S. Lippmann,^{a,b} Anita Mahadevan-Jansen^{b,c} and Rizia Bardhan^{*a}

a Department of Chemical and Biomolecular Engineering, Vanderbilt University, Nashville, TN 37212, USA. **b** Department of Biomedical Engineering, Vanderbilt University, Nashville, TN 37235, USA. **c** Biophotonics Center, Vanderbilt University, Nashville, TN 37232, USA.

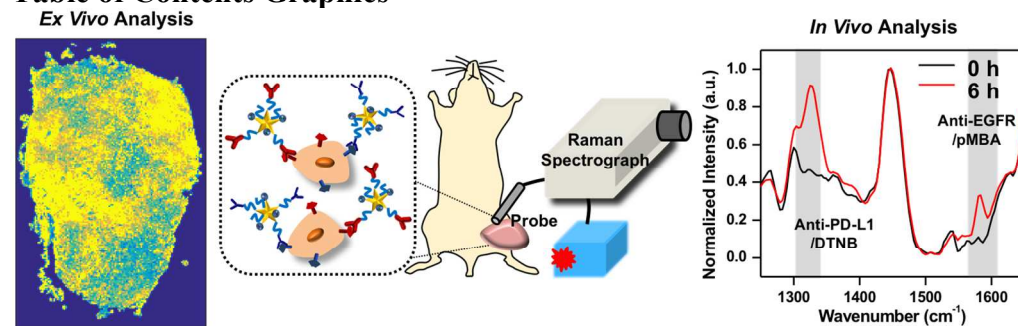
d Department of Radiology and Radiological Sciences, Vanderbilt University, Nashville, TN 37232, USA. **e** Vanderbilt University Institute of Imaging Science, Vanderbilt University, Nashville, TN 37232, USA. **f** Civil and Environmental Engineering, Vanderbilt University, Nashville, TN 37212.

*Corresponding Author

E-mail: rizia.bardhan@vanderbilt.edu

[†] Electronic supplementary information (ESI) available: TEM images of MDA-MB-231 cells incubated with AuNS, longitudinal SERS spectra of tumor xenograft without functionalized AuNS, *ex vivo* mapping of tumor xenograft at 1325 cm⁻¹ and 1580 cm⁻¹, tissue mask and sub-masks, pMBA intensity maps using tissue sub-masks, H&E analysis of the tumor xenograft and IC-PMS analysis of AuNS in major organs at 6 and 72h.

Table of Contents Graphics



Abstract

In this work, we demonstrate the targeted diagnosis of immunomarker programmed death ligand 1 (PD-L1) and simultaneous detection of epidermal growth factor receptor (EGFR) in breast cancer tumors *in vivo* using gold nanostars (AuNS) with multiplexed surface enhanced Raman spectroscopy (SERS). Real-time longitudinal tracking with SERS demonstrated maximum accumulation of AuNS occur 6 h post intravenous (IV) delivery enabling detection of both biomarkers simultaneously. Raman signal correlating to both PD-L1 and EGFR decreased by ~30% in control tumors where receptors were pre-blocked prior to AuNS delivery indicating both the sensitivity and specificity of SERS in distinguishing tumors with different levels of PD-L1 and EGFR expression. Our *in vivo* study was combined with the *first demonstration* of *ex vivo* SERS spatial maps of whole tumor lesions that provided both a qualitative and quantitative assessment of biomarker status with near cellular-level resolution. High resolution SERS maps also provided an overview of AuNS distribution in tumors which correlated well with the vascular density. Mass spectrometry showed AuNS accumulation in tumors, liver, and clearance via spleen, and electron microscopy revealed AuNS were endocytosed in tumors, Kupffer cells in the liver, and macrophages in the spleen. This study demonstrates SERS-based diagnosis mediated by AuNS provides an accurate measure of multiple biomarkers both *in vivo* and *ex vivo* which will ultimately enable a clinically-translatable platform for patient-tailored immunotherapies and combination treatment.

Keywords: gold nanoparticles, SERS, multiplex detection, programmed death ligand 1, *ex vivo* Raman mapping, immunoimaging

Introduction

T cells are an important effector of the immune system and are critical for inhibition of tumor development, growth, and invasion. Therefore, tumors evolve to evade immune surveillance by orchestrating a tumor microenvironment that suppresses productive antitumor immunity.^{1,2} The overexpression of immune checkpoint receptor programmed death protein-1 (PD-1), expressed in activated T cells, and the subsequent engagement of PD-1 to its ligand PD-L1 results in

inhibition of T cell proliferation, reduced secretion of effector cytokines, and immunosuppression.³ PD-L1 is upregulated in numerous tumor types including breast cancer,⁴ renal-cell cancer,⁵ non-small cell cancer⁶ and melanoma⁷ among others. This underscores the significance of PD-L1 as a predictive biomarker for immunotherapies. Inhibition of PD-L1 with therapeutic antibodies has shown to activate antitumor immunity and long term patient survival.⁸ ⁹ However, <25% of patients respond to PD-L1 blockade incurring high costs of unsuccessful therapies and toxic side-effects from prolonged antibody treatment.^{9, 10} Current clinical standards rely on immunohistochemistry (IHC) of biopsies, which often provide poor assessment of PD-L1 status in tumors. First, there are no clear criteria to define PD-L1 positivity by IHC which makes this approach prone to misinterpretation due to heterogeneous PD-L1 expression in inter- and intra-tumoral lesions.^{11, 12} Second, retrieval of PD-L1 antigen is also difficult in fixed tissue which results in significant variability in PD-L1 assay across clinical trials.¹³ Further, IHC of PD-L1 expression on archival tissue samples should be determined with caution, as prior treatment procedures can alter PD-L1 status in the tumor microenvironment.^{14, 15} And last, IHC is also limited in validation of multiple biomarkers in the same biopsy requiring repeated invasive procedures and patient discomfort. Therefore, a clinical need exists for noninvasive diagnostic tools that can both accurately identify PD-L1 *in vivo* and concurrently detect other biomarkers to identify patients who will respond to single checkpoint blockade, as well as accelerate clinical decisions by diagnosing patients who will benefit from combinatorial therapies.

In this work we address this critical need and demonstrate the diagnosis of PD-L1 *in vivo* and simultaneously diagnose EGFR (epidermal growth factor receptor) in triple negative breast cancer (TNBC) tumors. TNBC is a highly aggressive phenotype of breast cancer characterized

by the lack of estrogen receptor, progesterone receptor, and HER2/neu. Despite high rates of pathologic complete response after neoadjuvant chemotherapy, patient survival rates remain low. Recent work has shown TNBC tumors are highly immunogenic with high PD-L1 gene expression and higher rates of CD8⁺ T-cell infiltration than ER/PR positive breast cancer.¹⁶ Further, many TNBC tumors are known to overexpress EGFR, which is a transmembrane glycoprotein.¹⁷ The upregulation of EGFR promotes tumor progression by enhancing cell growth, angiogenesis, metastasis, and anti-apoptosis. Several EGFR-tyrosine kinase inhibitors, for example gefitinib and erlotinib, have demonstrated clinical efficacy in blocking the signal transduction pathways involved in tumorigenesis. Recent studies have also demonstrated that EGFR mutation status is directly correlated to the upregulation of PD-L1 which motivates us to diagnose both biomarkers with high sensitivity and specificity.¹⁸⁻²⁰ We have achieved this with noninvasive multiplexed surface-enhanced Raman spectroscopy (SERS) using gold nanostars (AuNS) labeled with targeting antibodies and Raman active molecules. SERS has rapidly emerged from a simple analytical technique to a preclinical screening tool for both qualitative and quantitative measure of biomarkers in tumors and for identification of cancerous cells.²¹⁻²³ SERS seamlessly enables multiplexed detection of multiple biomarkers due to the narrow linewidths of vibrational signatures of Raman molecules that can be simultaneously tracked both *in vivo* and *ex vivo*.²⁴⁻²⁶ The high spatiotemporal resolution of SERS has also enabled delineation of tumor margin from healthy tissue, and facilitated intraoperative tumor resection followed by identification of any residual disease.²⁷⁻²⁹

In this work we demonstrate longitudinal tracking of both PD-L1 and EGFR *in vivo* showing the localization of each marker with high sensitivity and specificity after intravenous delivery of AuNS in mouse models of TNBC. We note that whereas nanoparticles are often

intratumorally delivered *in vivo* to achieve high SERS signal,^{26, 30, 31} our approach of intravenous delivery is more clinically relevant for biomarker assessment. The strength of this work is *in vivo* time course study was combined with the *first demonstration* of *ex vivo* SERS maps of whole tumor lesions, that provided both a qualitative assessment of biomarker status and quantitative measure of their expression levels. High spatial resolution SERS maps also revealed distribution of AuNS in tumors that correlated well with highly vascularized areas of the tumor. Further, we examined the bioavailability and clearance of AuNS and corresponded those trends to *in vivo* endpoints. We anticipate the findings of this work will ultimately be extended to large animals and humans, and enable a clinically-translatable technology towards the emerging fields of immunoimaging and immunotherapies.

Materials and Methods

Synthesis of gold nanostars (AuNS)

Both (4-(2-hydroxyethyl)-1-piperazineethanesulfonic acid) (HEPES) and gold(III) chloride trihydrate (HAuCl₄) were purchased from Sigma-Aldrich. AuNS were synthesized through the one-step, seedless, HEPES-mediated method.³² First, 18 mL of Milli-Q water at 18 MΩ was mixed with 12 mL of 270 mM HEPES (pH 7.40 ± 0.2) by gentle inversion. Next, 300 μL of 20 mM chloroauric acid (HAuCl₄) was added. The solution was left undisturbed at room temperature and reacted for 75 minutes.

Functionalization of gold nanostars (AuNS)

SERS tags, 4-mercaptobenzoic acid (pMBA) and 5,5'-Dithiobis(2-nitrobenzoic acid) (DTNB) were purchased from TCI America. Methoxy-polyethylene glycol-thiol (mPEG-SH, M_w 5000) and orthopyridyl-disulfide poly(ethylene glycol)-N-hydroxysuccinimide ester (OPSS-PEG-NHS ester, M_w 2000) were purchased from JenKem Technology. To conjugate Raman tags to the

AuNS surface, pMBA or DTNB were dissolved in 100% ethanol. Small concentrated volume (6 μL of 10 mM) of pMBA or DTNB solution was added to 60 mL of AuNS and reacted for 10 minutes with constant stirring at 4 $^{\circ}\text{C}$. The solution was centrifuged at 6000 rpm for 10 minutes to remove excess, unreacted Raman tag. To bind active targeting antibody to AuNS, OPSS-PEG-NHS linkers were first reacted with the monoclonal antibodies, Human EGF R/ErbB1 antibody (antiEGFR, R & D Systems) or Human CD274 (B7-H1, PD-L1) antibody (antiPDL1, BioLegend). Briefly, lyophilized OPSS-PEG-NHS was dissolved in 100 mM pH 8.6 \pm 0.1 sodium bicarbonate (NaHCO_3) buffer at a concentration of 160 mg/mL. Note, high pH is crucial for ester and amine chemistry in forming amide bonds. As a result, the antibody chemistry was tailored to achieve this desirable pH. At 1:9 volume ratio, 72 μL of 1 mg/mL antiEGFR antibody (reconstituted in pH 8.6 NaHCO_3 buffer) was added to 8 μL of OPSS-PEG-NHS solution. AntiPDL1 antibody was received at pH 7.4 phosphate buffer saline. To maintain the favorable pH for linker-antibody reaction, OPSS-PEG-antiPD-L1 was prepared in the concentration and volume ratio as with the OPSS-PEG-antiEGFR reaction, but it was further diluted 5-fold with pH 8.6 NaHCO_3 . The OPSS-PEG-antibody chemistry was performed on an inverter at 4 $^{\circ}\text{C}$ for 24 h.

After the OPSS-PEG-antibody reaction was completed, 80 μL of OPSS-PEG-antiEGFR or OPSS-PEG-antiPDL1 was added to 6 ml of Raman tag-labeled-AuNS (DTNB-AuNS or pMBA-AuNS) at 1.14 mg/mL. Antibody-AuNS solution was left on an inverter at 4 $^{\circ}\text{C}$ and reacted for 24 h. Post 24 h antibody-AuNS reaction, an additional layer of polyethylene glycol (mPEG-SH, M_w 5000) chemistry was performed to passivate any free surface area on the gold, neutralize surface charge, and provide particle stability. Briefly, 700 μL of 5 μM mPEG-SH was added to the AuNS solution and mixed for 10 minutes at room temperature. Lastly, the functionalized AuNS (antiEGFR-pMBA-AuNS or antiPDL1-DTNB-AuNS) were centrifuged at

4000 rpm for 10 minutes. The pellet was then resuspended in sterile phosphate buffered saline (pH 7.40 ± 0.1) at 6 mg/mL.

Characterization of functionalized AuNS

A 2:1 mixture of antiEGFR-pMBA-AuNS and antiPD-L1-DTNB-AuNS were visualized using an Osiris transmission electron microscope (TEM) at 200 keV. Plasmon resonance of AuNS and functionalized AuNS were monitored with a Varian Cary 5000 UV-Vis NIR spectrophotometer. Raman spectra of antiEGFR-pMBA-AuNS, antiPD-L1-DTNB-AuNS, and the 2:1 mixture were obtained by using the custom portable Raman setup with a 785 nm laser.

MDA-MB-231 Xenograft Model and *in vivo* SERS Raman Imaging

All animal procedures were followed and approved by Vanderbilt University Medical Center Animal Care and Use Program (IACUC #M1600097-00). Athymic nude mice at 3-4 week old (Hsd: Athymic Nude-Foxn1^{nu}; Envigo) were used in this study. MDA-MB-231 cells were cultured in Dulbecco's Modified Eagle's medium (DMEM, Gibco) supplemented with 10% fetal bovine serum (FBS, Denville Scientific). The cells were maintained at 37 °C and 5% CO₂ and were cultured at least two weeks prior to injection into mice. The cells were diluted 1:1 with matrigel (GFR Membrane Matrix, Corning). One million MDA-MB-231 cells per 100 µl were injected into the left mammary fat pad of each mouse. The tumor was monitored with calipers every two days. SERS experiments started once the tumor reached 5 mm in diameter. SERS spectra of 5 different spots of the tumor xenograft were measured with 10 s acquisition time before functionalized AuNS were injected (0 h). Functionalized AuNS, antiEGFR-pMBA-AuNS and antiPDL1-DTNB-AuNS at 2:1 ratio were injected retro-orbitally. Raman measurement was done at 6, 12, 24, 48 and 72 h post particle injection. For each time point, mice were anesthetized with isoflurane. All room lights were turned off during SERS measurement. The Raman fiber

optic probe was gently placed on the tumor xenograft for a spectral measurement (1 s acquisition time per spectrum with 10 accumulations). A 785 nm near-infrared diode laser (Innovative Photonics Solutions) was operated at 80 mW. A neon-argon lamp, acetaminophen, and naphthalene were used as standards to calibrate the absolute and relative wavenumber axis of the system in determining and calculating Raman shifts. Raman scattering was collected with an imaging spectrograph (Kaiser Holospec), and a -70 °C cooled CCD camera (Princeton Instruments) was used to capture the data, which was further processed by the connected computer system.

All obtained spectra were processed through steps including spectral response calibration with a NIST calibrated lamp, smoothing using a (2,7) Savitzky-Golay filter, and background subtraction using a modified (7th order) polynomial fit method.³³⁻³⁶ To clearly visualize the appearance of DTNB and pMBA peaks, 1325 cm^{-1} and 1580 cm^{-1} were normalized to the biological peak, 1440 cm^{-1} at each time point. For pre-block control, mice were injected (IP) with 200 μg of antiEGFR antibody and 200 μg of antiPDL1 antibody (1 mg/mL in pH 7.40 ± 0.1 phosphate buffered saline) 2 h before functionalized AuNS injection. Note, the antibodies used for pre-blocked controls were the same products used to functionalize the active targeting AuNS. Raman measurement for the pre-block control group was performed in the same manner as the experiment group.

Inductively coupled plasma-mass spectrometry (IC-PMS)

Mice bearing MDA-MB-231 cells were injected with functionalized AuNS, antiEGFR-pMBA-AuNS and antiPDL1-DTNB-AuNS at 2:1 ratio. Per mouse, the tumor, stomach, liver, spleen, kidneys, heart, lungs, and brain were retrieved at maximum accumulation time (6 h post particle

injection) or at the end of the study (72 h post particle injection) and were frozen immediately in liquid nitrogen.

Sample Preparation:

Tumors and major organs were then freeze dried using a lyophilizer. Next, acid digestion was used to dissolve gold contents. Dried tumors and organs were placed in scintillation vials and weighed. Trace metal grade HCl (Fisher, A508-P500) and HNO₃ (Fisher, A509-P500) were used to prepare 75 vol. % aqua regia (4:1 volume ratio HCl: HNO₃), which was then added to the organ/tumor. Samples were soaked in aqua regia for 72 h. Aqua regia was then boiled off with gentle heating. The semi-dried samples were re-dissolved in 10 ml of 2 vol. % aqua regia. Impurities were removed with syringe filtering prior to IC-PMS reading. Organs with high gold accumulation: liver, spleen, and tumor were further diluted 10-fold with 2 vol. % aqua regia.

IC-PMS Analysis

IC-PMS measurements of aqueous samples were carried out at Vanderbilt University, Department of Civil and Environmental Engineering. Perkin Elmer model ELAN DRC II in standard mode was used for readings. A six-point calibration curve between approximately 0.05 µg/L and 500 µg/L was used for gold isotope 197. For every 3-5 samples, analytical blanks and analytical check standards (0.5 µg/L) were measured and confirmed to be within 15% of the specified value. The instrument was set at 1.5 kW radio frequency (RF) power, 15 L/min argon plasma flow, 1 L/min nebulizer flow, and 1 s integration time for 3 replicates.

Transmission electron microscope imaging of tumor and organs

Mice bearing MDA-MB-231 cells were injected with functionalized AuNS, antiEGFR-pMBA-AuNS and antiPDL1-DTNB-AuNS at 2:1 ratio. SERS spectra were measured at 6 h post particle injection to ensure the increase in DTNB/pMBA signal was observed. The mouse was then

sacrificed, and the tumor xenograft was retrieved. Additionally, the heart, liver, and spleen of a different set of mice were removed 72 h post functionalized AuNS injection to evaluate the clearance of the particles. Samples were fixed in 2.5% glutaraldehyde in 0.1M cacodylate buffer (pH 7.4 ± 0.1) at room temperature for 1 h and then 24 h at 4 °C. Specimens were processed for transition electron microscopy (TEM) and imaged in the Vanderbilt Cell Imaging Shared Resource-Research Electron Microscopy facility.

Sample Preparation

The samples were fixed with 1% osmium tetroxide for 1 h at room temperature and further washed with 0.1 M cacodylate buffer. Dehydration was done through a graded ethanol series. Next, 3 exchanges of 100% ethanol and 2 exchanges of pure propylene oxide (PO) were performed. Subsequently, 25% Epon 812 resin and 75% PO were used to infiltrate the samples for 30 min at room temperature. They were then infiltrated with 50% Epon 812 resin and 50% PO for 1 h and overnight, respectively. The samples went through a Epon 812 resin and PO (3:1) exchange for 4 h and finally were incubated with pure epoxy resin overnight. Lastly, two changes of pure epoxy resin were used to embed the samples. Polymerization was done for 2 days at 60 °C.

Sectioning and Imaging

Ultra-structure identification was first achieved with thick sections at 500-1000 nm. Once regions of interest were identified, 70-80 nm ultra-thin sections were cut. Samples were placed on 300-mesh copper grids and were stained with 2% uranyl acetate, followed by Reynold's lead citrate. The final tissue samples were imaged with the Philips/FEI Tecnai T12 electron microscope.

Ex vivo Raman Mapping.

Mice bearing MDA-MB-231 were injected with functionalized AuNS (antiEGFR-pMBA-AuNS and antiPDL1-DTNB-AuNS at 2:1 ratio) retro-orbitally. The tumor xenograft was retrieved and cryo-embedded 6 h post particle administration. Frozen tumor samples were cryo-sectioned on CaF₂ disks by Vanderbilt University TPSR (5 μ m thick). Samples were thawed at 4 °C overnight and then room temperature for 2 h prior to Raman mapping. Montages of brightfield images were obtained with a 20x (NA) objective. A rectangular Raman map with a 50 μ m step size was acquired with 10 s integration time, L50x objective (NA), and a 785 nm laser (30 mW). After the Raman spectra for the entire map were obtained, cosmic ray removal with nearest neighbor method was implemented. A custom MATLAB code was used to perform smoothing and biological fluorescent background subtraction. Smoothing of the data was done by following the Savitzsky and Golay method with 5th order and coefficient value of 61. Modified polyfit method was performed to subtract the background fluorescence. A polynomial with 9th order was used to fit the Raman spectra with threshold of 0.0002. The Raman map was then generated with wavenumber of interest (DTNB = red, pMBA = green).

To obtain quantitative analysis of both pMBA and DTNB, the raw biological peak (1440 cm^{-1}) was selected to generate the masks of whole tissues. The pixels were assigned as a part of a mask when their intensities were higher than a specified threshold. A Gaussian function was applied to the mask images to smooth the edges ($\sigma = 20 \mu\text{m}$). The residuals and the holes in the images were removed and filled (area opening algorithm), respectively. The final masks were compared with the optical images to ensure the authenticities. The sub-masks of high- and low-intensity groups were obtained in a similar fashion from the processed (smoothed and baseline corrected) images of biological peak. These masks were separated according to a threshold and are processed with necessary smoothing, removing, and filling. Tissue mask and sub-masks were

then applied to 1325 cm^{-1} and 1580 cm^{-1} for each individual tag. As a result, the Gaussian model mean and sigma can be obtained.

Statistical Analysis

Statistical differences were evaluated with Student's t tests. All data are presented as mean \pm standard deviation.

Results and discussion

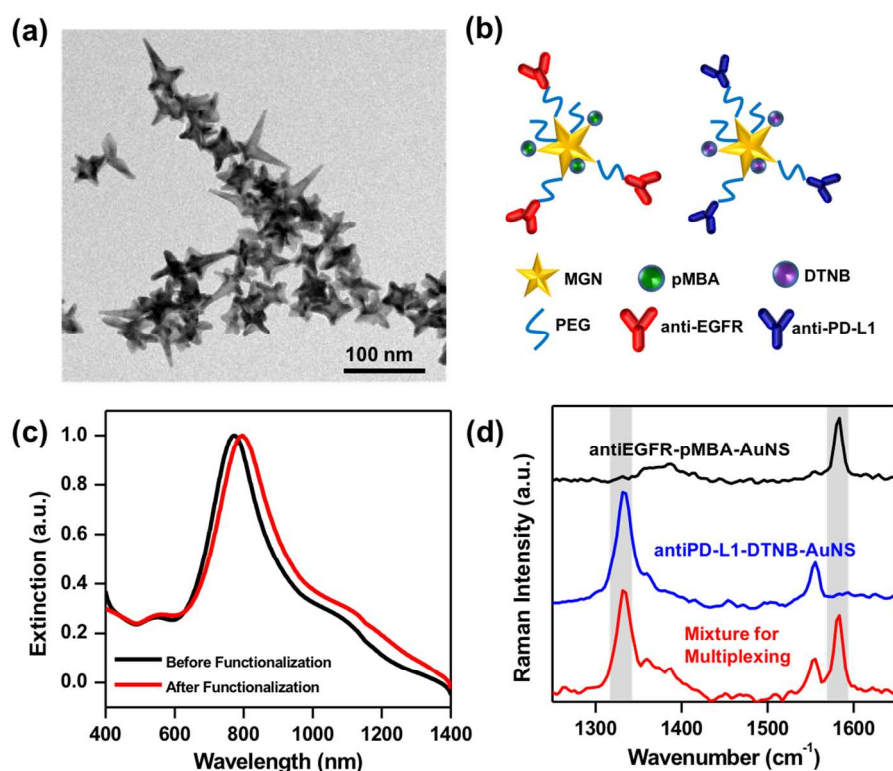
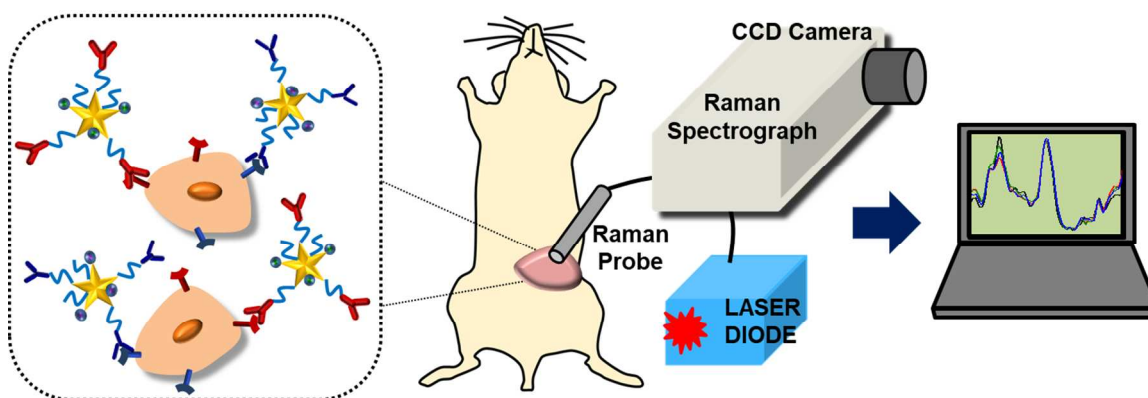


Figure 1. Characterization of functionalized AuNS. (a) TEM image of antibodies and Raman tag functionalized AuNS showing the anisotropic structure and sub-100 nm size of AuNS. (b) Schematic representation of AuNS functionalized with Raman-active tag, pMBA or DTNB. Each Raman tag pairs with a targeting antibody, anti-EGFR with pMBA and anti-PD-L1 with DTNB. (c) Extinction spectra of AuNS before (bare AuNS) and after functionalization (with

Raman tag and targeting antibody). (d) Raman spectra of antiEGFR-pMBA-AuNS, antiPDL1-DTNB-AuNS and a 2:1 mixture. The Raman peaks of interest of both pMBA and DTNB are highlighted in gray.

Gold nanostars (AuNS) were synthesized by a one-step seedless method as described in our previously published procedure.^{32, 37, 38} The biological buffer, HEPES (2-[4-(2-hydroxyethyl)piperazin-1-yl]ethanesulfonic acid) is used as both a capping and reducing agent, enabling shape-controlled synthesis. Gold nanoparticles synthesized via biological buffer or peptides are biocompatible with minimal toxicity.^{37, 38} The sub-100 nm size of AuNS (~50-70 nm tip-to-tip dimension (Fig. 1a)) allows AuNS to accumulate in the tumor microenvironment through the enhanced permeability and retention effect (EPR), thus increasing the likelihood of endocytosis by cancer cells.^{39, 40} The unique structure of AuNS gives rise to the “nanoantenna effect” where the spherical cores absorb incident light and route it to the protrusions where strong electromagnetic field are concentrated at the tips.^{32, 41, 42} These intense near-field enhancements at the tips of AuNS amplify the vibrational signal of proximal Raman molecules by 9 – 10 orders of magnitude enabling high resolution SERS.^{42, 43} In this work, we show the multiplexed detection of biomarkers PD-L1 and EGFR through SERS by conjugating Raman tags and monoclonal antibodies specific to these biomarkers onto AuNS surface (Fig. 1b). We generated two sets of bioconjugated AuNS, PD-L1 targeting set was labeled with Raman tag 5,5-dithio-bis-(2-nitrobenzoic acid) (DTNB) and anti-PD-L1 monoclonal antibodies, and EGFR targeting set was labeled with Raman tag para-mercaptobenzoic acid (pMBA) and anti-EGFR antibodies. Both DTNB and pMBA were covalently linked to AuNS surface via a thiol group. Monoclonal antibodies were conjugated with AuNS via OPSS-PEG2000-NHS linkers where the thiols on the orthopyridyl (OPSS) group bind to AuNS, and the N-hydroxysuccinimide (NHS) ester group forms an amide bond via the primary amines of the antibodies. Lastly, a layer of

thiolated-polyethylene glycol was added to AuNS surface to ensure charge neutrality, reduce uptake by the mononuclear phagocytic system (MPS), and to provide *in vivo* stability. The biofunctionalization of AuNS resulted in a ~ 25 nm shift in the plasmon resonance (Fig. 1c) indicative of an increase in the particle size as well as change in refractive index of the medium. The plasmon resonance of functionalized AuNS was controlled in the near-infrared region (650–900 nm) to enable enhanced tissue penetration and deep tissue imaging. The Raman spectra of the functionalized AuNS were acquired using a custom Raman system with a 785 nm continuous wave laser (Fig. 1d). The signature peak of antiEGFR-pMBA-AuNS is at 1580 cm^{-1} , which corresponds to the ring stretching mode of pMBA.⁴⁴ The dominant peak, 1325 cm^{-1} of antiPD-L1-DTNB-AuNS is attributed to the symmetric stretching mode of the nitro group of DTNB.⁴⁵ For multiplexed SERS a 2:1 ratio of antiEGFR-pMBA-AuNS: antiPD-L1-DTNB-AuNS was employed since the peaks of interest for DTNB and pMBA have comparable Raman intensities at this ratio. Furthermore, due to their distinct Raman fingerprints and narrow linewidths, both pMBA and DTNB are easily distinguishable enabling multiplexed detection of PD-L1 and EGFR *in vivo*. To confirm the receptor-antibody binding, we incubated the MDA_MB-231 cells with a mixture of antiEGFR-pMBA-AuNS: antiPD-L1-DTNB-AuNS. After 16 h of incubation, TEM micrographs showed most of the AuNS were bound to the surface of the cancer cells with minimal endocytosis (Fig. S1†).



Scheme 1. Schematic representation of *in vivo* SERS setup where nude mice bearing MDA-MB-231 xenografts were administered a mixture of antiEGFR-pMBA-AuNS and antiPD-L1-DTNB-AuNS via retro-orbital injections. A custom-built portable Raman setup was used for SERS measurement consisting of a 785 nm continuous-wave laser diode, a spectrograph, CCD camera, and fiber-optic probe.

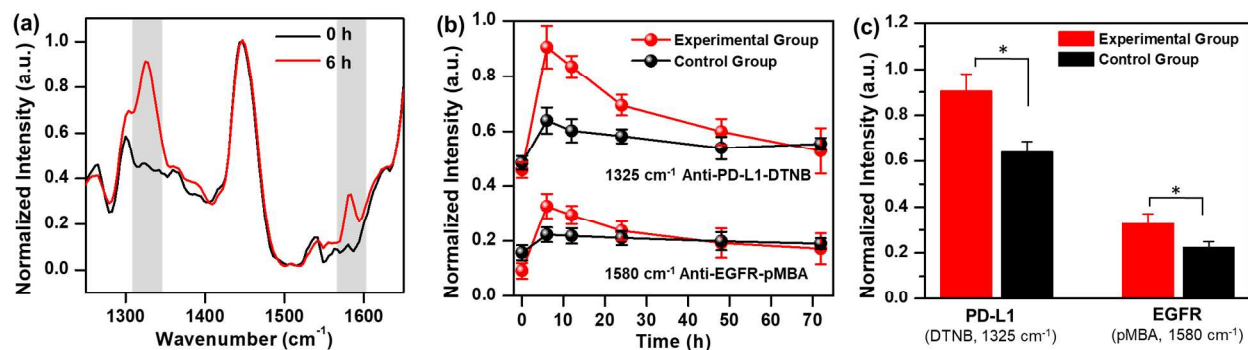


Figure 2. Multiplexed SERS longitudinal study. (a) Averaged, normalized Raman spectra of tumors ($n=4$) were plotted before (0h) and at maximum accumulation time point, 6h-post functionalized AuNS injection. The appearance of SERS signal of the signature peaks for both pMBA (1580 cm^{-1}) and DTNB (1325 cm^{-1}) are indicated by gray boxes. (b) Longitudinal SERS ($n=4$) performed at 6, 12, 24, 48 and 72 h post particle injections where pMBA and DTNB signals were normalized to 1440 cm^{-1} biological peak. In the control group both markers were pre-blocked with monoclonal antibodies 2h prior to delivery of functionalized AuNS. (c) SERS intensity comparison of experimental and control group tumors at 6h time-point showing that for both PD-L1 and EGFR detection, SERS signal decreased by $\sim 30\%$ ($p < 0.0005$) in the control group.

Multiplexed *in vivo* SERS was performed by administering the mixture of functionalized AuNS via retro-orbital injections to nude mice bearing MDA-MB-231 triple negative breast cancer xenografts. Whereas SERS-active nanoparticles have been commonly delivered *in vivo*

via intratumoral^{26, 31} or subcutaneous³⁰ delivery, we found systemic injection is necessary for tracking AuNS longitudinally to assess receptor status. Furthermore, systemic delivery is clinically-translatable enabling us to understand the uptake, biodistribution, and clearance of AuNS, and the overall sensitivity and specificity of our approach for multiplexed detection of biomarkers. We also note that whereas multiplexed *in vivo* SERS has been shown previously, longitudinal tracking of SERS-active nanoparticles at different time-points has not been effective.^{24, 46} We performed SERS at 6, 12, 24, 48 and 72 h post AuNS delivery with a custom Raman setup described in the methods section.^{47, 48} The fiber optic Raman probe was gently placed on top of the mammary xenograft to acquire one second acquisitions with ten accumulations. A 785 nm continuous-wave laser was used at 80 mW and SERS measurements were obtained at five different spots on the tumor and the spectra were then averaged. The acquired Raman spectra were processed with fluorescence subtraction to remove biological autofluorescence and then normalized to the 1440 cm⁻¹ biological peak (Scheme 1). The 1440 cm⁻¹ biological band (CH vibrations for both lipid and protein) has minimal change during time-course study in the same mouse shown in supporting information (Fig. S2†) serving as an excellent internal reference. To evaluate the changes in the intensity of Raman peaks, baseline Raman spectra of the tumor xenograft were also acquired immediately prior to the functionalized AuNS injection (0 h). Both signature peaks of DTNB (1325 cm⁻¹) and pMBA (1580 cm⁻¹) increased significantly and reached a maximum at 6 h post AuNS delivery as observed in our longitudinal study (Fig. 2a). Averaged of five spectra across different locations of the tumor from each mouse (n=4 total mice) are shown in SI (Fig. S3†). By tracking the Raman spectral features of DTNB and pMBA during time-course study, the simultaneous targeted detection of checkpoint ligand PD-L1 and biomarker EGFR is assessed *in vivo*. Maximum accumulation of

AuNS occur at ~ 6 h, and between 48 h to 72 h both DTNB and pMBA signals returned to baseline levels (Fig. 2b), indicating the clearance of AuNS via mononuclear phagocyte system of liver and spleen. To demonstrate both the sensitivity and specificity of functionalized AuNS in targeted detection of EGFR and PD-L1, we pre-blocked both biomarkers as our negative control. Prior work in the literature has effectively demonstrated that antibody dosage can successfully block receptors in mice tumors.⁴⁹⁻⁵² We injected 200 μ g of monoclonal antibodies (anti-EGFR and anti-PD-L1) via intraperitoneal injection (IP) 2h prior to injection of functionalized AuNS to saturate the surface receptors and block the binding of functionalized AuNS to these biomarkers. Longitudinal SERS comparing the experimental group with the control group tumors (Fig. 2b-c) showed statistically significant differences in both PD-L1, corresponding to DTNB signal which decreased by 31% ($p < 0.0005$), and EGFR, corresponding to pMBA signal which decreased by 32% ($p < 0.0005$). The observed differences in SERS signal in longitudinal measurements between experimental and control groups demonstrate (1) the specificity of our approach in rapid and accurate targeted detection of PD-L1 and EGFR *in vivo*, and (2) the sensitivity of our approach as AuNS amplify the SERS signal of Raman reporters sufficiently to provide an assessment of receptor expression on tumor surface.

Multiplexed *in vivo* monitoring of PD-L1 and EGFR has several advantages over the current standard measure i.e. immunohistochemistry (IHC) of invasive biopsies. First, *in vivo* measurements track biomarker status of whole tumor lesions which reduces misinterpretation due to inter- and intratumoral heterogeneity. Second, it allows monitoring of biomarker expression during the course of disease minimizing the need for repetitive biopsies and patient discomfort. This is of particular clinical relevance as both PD-L1 and EGFR expression in patients are known to alter with prior treatments. Third, *in vivo* SERS enabled by systemic

delivery of contrast agents such as functionalized AuNS takes into account multiple factors such as vascular permeability, blood vessel density, necrotic regions providing a more comprehensive assessment of PD-L1/EGFR expression than the qualitative “yes or no” type of information available through IHC. We are not suggesting *in vivo* SERS should replace IHC, which is a gold standard in clinical histopathology, but rather supplement IHC to obtain a more accurate and reliable prognosis enabling patient-tailored treatment strategies.

In vivo SERS is ideal for rapid molecular identification of biomarkers specifically for subcutaneous tumors where the penetration-depth of near-infrared light and detection of Raman scattering is less affected by the tissue characteristics. However, for clinical translation of this technology, SERS should benefit patients with both early-stage and late-stage cancer. Whereas current clinical pathology mostly relies on IHC, it is inherently subjective, often misinterpreted when presented with highly heterogeneous tumors, and limited in multiplexed validation of multiple biomarkers in the same biopsy. Other *ex vivo* techniques, such as immunofluorescence (IF), have enabled quantitative assessment of biomarkers; however, tissue autofluorescence and rapid photobleaching of commonly used fluorescent tags make this approach unreliable. Therefore, in addition to *in vivo* SERS imaging, here we show that *ex vivo* Raman maps of tumor sections is a powerful approach combining high spatial and temporal resolution, and address some of the current challenges with IHC and IF. Tumors were retrieved at the maximum accumulation time-point (6h post AuNS delivery), cryo-fixed, sectioned at 5 μm thickness, and transferred to calcium fluoride (CaF_2) disks to minimize Raman signal from the substrate. A brightfield image of the tissue was recorded (Fig. S4a†) to show tumor sections retain their morphology on CaF_2 disks. We performed SERS maps of an entire tissue section at 50 μm step size (50 μm in both x and y direction), providing near cellular-level resolution. The tissues were

excited with a 785 nm laser at 30 mW using a 50x objective with 10 s acquisitions. SERS spectra were processed to remove cosmic rays, subtract tissue autofluorescence, and subsequently intensities of DTNB and pMBA were plotted such that each pixel generated a color map assigned with an RGB color - red for DTNB (1325 cm^{-1}) and green for pMBA (1580 cm^{-1}) (Fig. S4b†). The intensity map shown in figure 3a provides an overview of localization of the functionalized AuNS, antiEGFR-pMBA-AuNS and antiPD-L1-DTNB-AuNS, where the signal from each Raman tag can be correlated to the respective biomarkers targeted. We then identify regions of interest (Fig. 3ai, ii) in the spatially-resolved Raman map of the tissue to qualitatively assess biomarker status. High magnification SERS maps (Fig. 3b) show near cellular-level resolution of tumor areas that are PD-L1 rich (Fig. 3bii-2), EGFR rich (Fig. 3bii-3), rich in both biomarkers (Fig. 3bii-4), as well as likely necrotic areas where AuNS did not accumulate (Fig. 3bi-1, no signal). The corresponding SERS spectra from these regions of interest confirm the biochemical footprint of PD-L1 and EGFR targeted AuNS distribution (Fig. 3c).

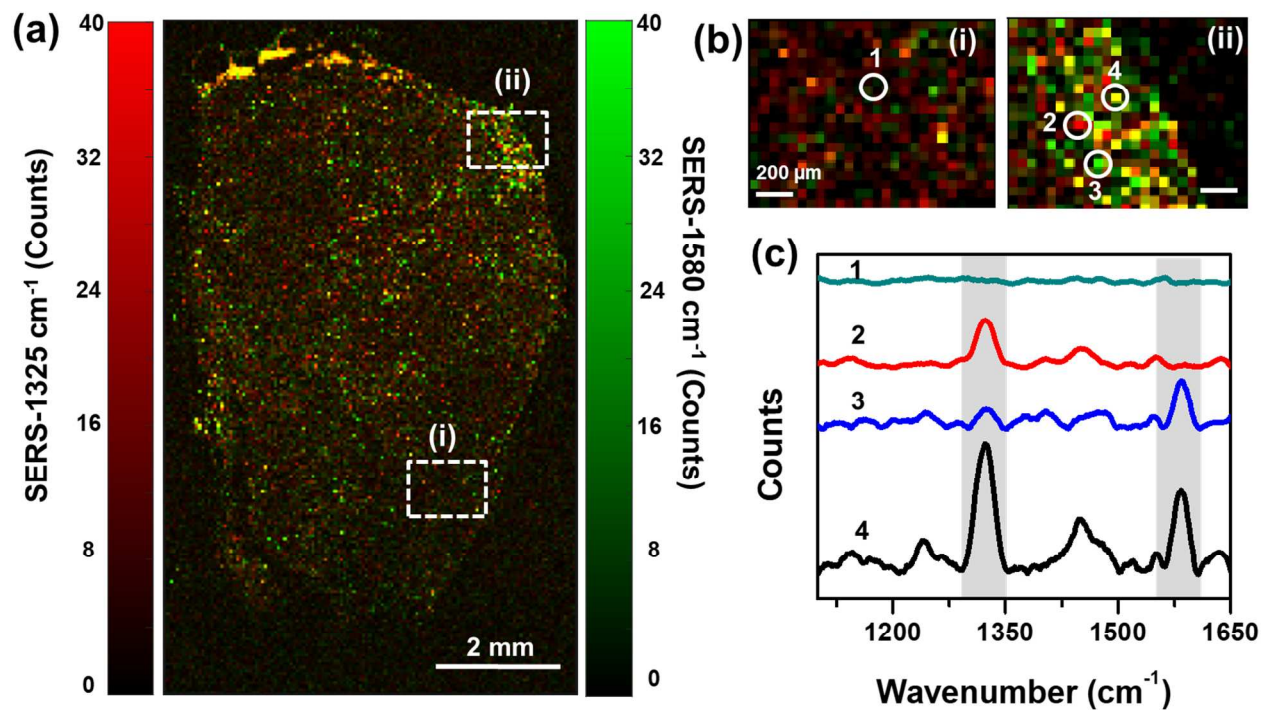


Figure 3. *Ex vivo* Raman spatial maps of breast cancer tumor sections. (a) SERS intensity map of the entire tissue section performed at 50 μm per pixel showing an overlap of both DTNB (1325 cm^{-1}) and pMBA (1580 cm^{-1}) signals. Specific regions of interest (ROI) are indicated. (b) High magnification SERS intensity map from the ROIs indicated in 'a' showing (i) tissue region with minimal AuNS accumulation and no Raman signal, (ii) tissue region with high AuNS accumulation indicating PD-L1 and EGFR expression. (c) Corresponding Raman spectra indicating (1) no AuNS binding, (2) PD-L1 rich area, (3) EGFR rich area, and (4) both EGFR and PD-L1 rich area (DTNB and pMBA signature peaks are indicated by grey boxes).

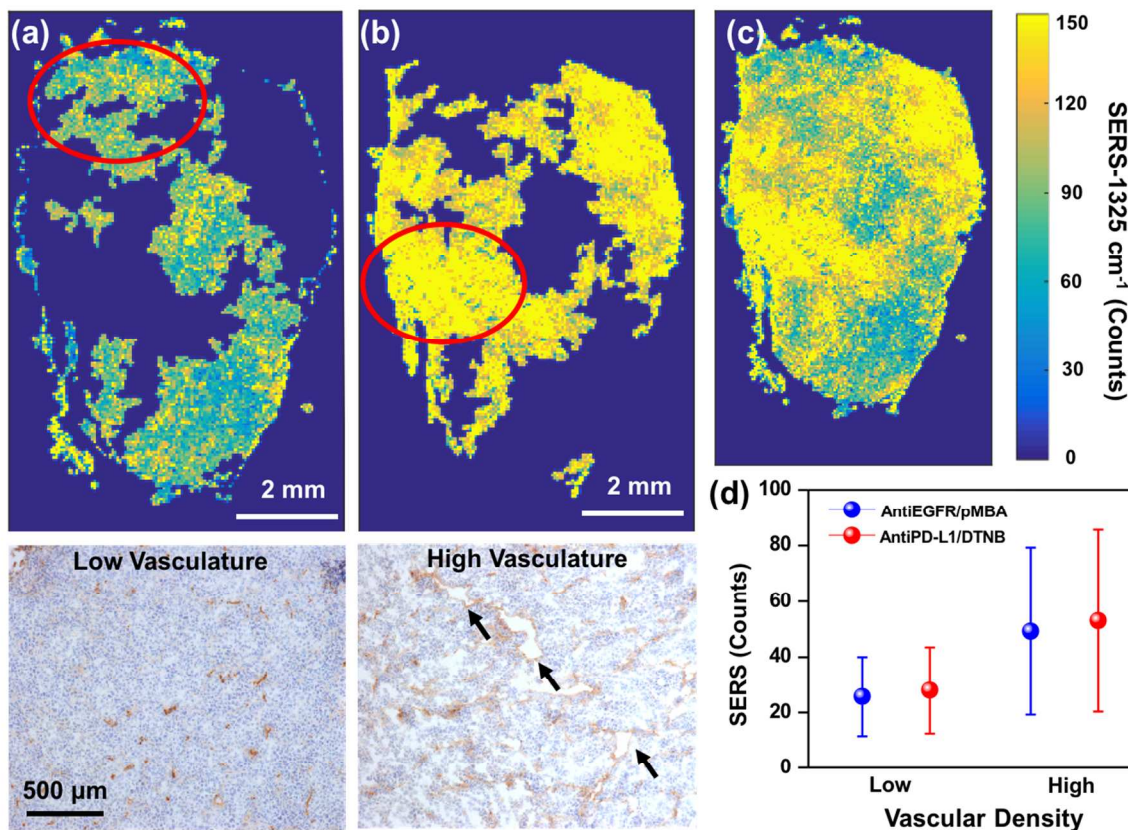


Figure 4. Analysis of receptor status via Raman spatial maps of tumor sections at 1325 cm^{-1} corresponding to antiPD-L1/DTNB/AuNS. The biological peak was fit to two Gaussian functions to distinguish areas with high and low SERS intensity. (a) Low SERS intensity map and corresponding CD31 staining (bottom) of the circled area showing poorly vascularized area of the tissue. (b) High SERS intensity map and corresponding CD31 staining (bottom) of the circled area showing high vascular density. The micro vessels are indicated by the black arrows. (c) Overlay of (a) and (b) provides an overall SERS spatial map and a color bar indicating intensities. (d) Quantitative assessment of both antiPD-L1/DTNB/AuNS and antiEGFR/pMBA/AuNS in low and high vascularized areas identified by using a model of two Gaussian functions to the peaks of interests of the intensity maps.

Nanoparticle accumulation in tumors through surface receptor binding and through the EPR effect is known to occur in well-vascularized areas.⁵³⁻⁵⁵ Therefore, by comparing the Raman intensities of both DTNB and pMBA in the tissue maps to the vascular density, we demonstrate the accuracy of our approach where functionalized AuNS should accumulate in the high vascular density areas with high SERS intensity. Conversely, low accumulation of AuNS is attributable to poorly vascularized or necrotic regions of the tumor which should correspond to low SERS intensity. We generated a SERS distribution map (Fig. 4a-c) using the 1440 cm^{-1} biological peak, which remains constant throughout the tumor, to obtain a tissue mask. This mask blocks out all the empty/no-tissue areas (SI Fig. 4a) and enables generation of Gaussian distributions of both DTNB (1325 cm^{-1}) and pMBA (1580 cm^{-1}). By fitting the biological peak intensities (1440 cm^{-1}) throughout the tumor with two Gaussian functions, low and high Raman intensity regions were generated with high confidence ($R^2 = 0.995$, Fig. S5b,c†). Tissue sub-masks of high and low SERS intensity regions of DTNB and pMBA were then generated by setting a threshold and by fitted using the two Gaussian functions. A 2-dimensional (2D) Gaussian filter ($\sigma = 20\ \mu\text{m}$) was also applied to prevent any extreme pixels for biased results. By applying the tissue sub-masks to the DTNB Raman signal map, low (Fig. 4a top), high (Fig. 4b top), and combined (Fig. 4c) SERS distribution maps were generated with good fits to the distribution of the SERS signal ($R^2 = 0.983$ for high intensity, and $R^2 = 0.999$ for low intensity). These high and low SERS intensity maps are useful in visualizing regions of the tissue to assess their state of angiogenesis or necrosis. Vascular staining was performed with endothelial cell marker CD31 to confirm the degree of angiogenesis in the tumor tissue and correlate to the SERS intensity of DTNB and pMBA which directly corresponds to AuNS accumulation. We observed that high SERS intensity areas correlate strongly to well-vascularized areas where the blood vessels are indicated

by arrows in figure 4b. However, low SERS signal regions of the tissue did not have abundant vascular density (Fig. 4a bottom) clearly indicating that AuNS accumulation and resulting SERS signal overlaps with the vascular density of the tumor. SERS intensity distribution maps for pMBA presents similar results as the DTNB maps (Fig. S6†). The spatial information provided by the Raman maps enables us to provide a quantitative assessment of biomarkers to understand the heterogeneity of receptor expression both inter- and intra-tumorally. We retrieved $n = 3$ mouse tumors at maximum accumulation time-point (6h post AuNS injection) and performed SERS mapping and obtained the mean intensity of DTNB and pMBA for each tumor section to generate low and high signal areas corresponding to low and high accumulation of AuNS. The quantitative (Fig. 4d) assessment of functionalized AuNS distribution shows (i) there is a significant difference between the SERS intensity in high vascularized and low vascularized areas, but (ii) there is no significant difference in expression between EGFR or PD-L1 receptor throughout this tumor. This is expected as both EGFR and PD-L1 are in abundance in MDA-MB-231 cells and differences in expression levels in individual tumor sections cannot be easily detected.

The SERS maps of tumors *ex vivo* provides (i) a qualitative assessment of both PD-L1 and EGFR confirming multiplexed biomarker status in the same tissue section, which cannot be assessed with IHC; (ii) a distribution map of functionalized AuNS accumulation in the tumor that can be strongly correlated to the vascular density indicating the high accuracy of our approach and that AuNS localize in well-vascularized areas through both receptor-mediated endocytosis and EPR effect; (iii) spatially-resolved quantitative analysis of both PD-L1 and EGFR expression levels in the same tissue section that allows us to determine heterogeneities in receptor status; and finally (iv) SERS provides a highly reliable approach for both *in vivo* and *ex vivo*

measurement since it is undeterred by tissue autofluorescence or photobleaching, which typically plagues IF-based methods. These collective attributes of SERS mediated by immunoactive AuNS will ultimately enable patient-selection for PD-L1 checkpoint blockade as well as identify those who will respond to combination PD-L1/EGFR treatment to improve breast cancer patient outcome, as well other cancers where these biomarkers are upregulated.

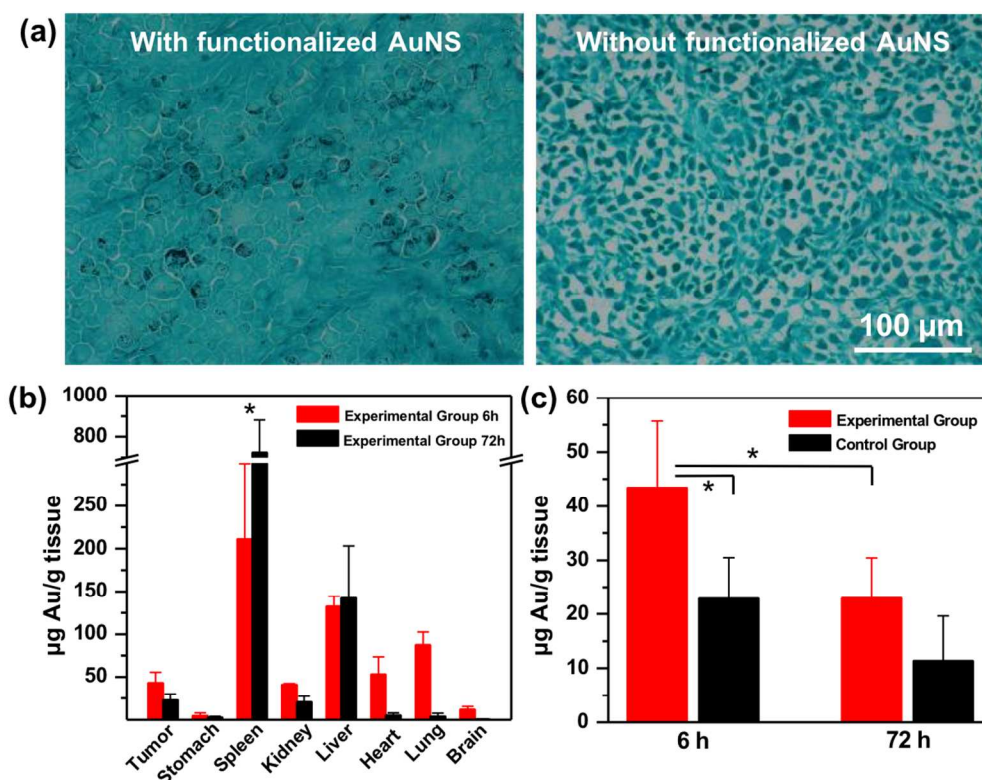


Figure 5. Distribution of AuNS functionalized with Raman tags, antibodies, and PEG. (a) Silver enhancement stain showing AuNS accumulation in tumors vs. tumors that did not receive AuNS. AuNS appear as dark spots in silver enhancement stain. (b) IC-PMS results of Au content in tumor and major organs at 6 h (n=3) and 72 h (n=4) post IV delivery of functionalized AuNS showing AuNS presence in tumor and in the mononuclear phagocyte system. The difference in Au content of spleen at 6 h and at 72 h is statistically significant ($p < 0.05$). (c) IC-PMS analysis of AuNS accumulation in tumors compared at 6 h and 72 h. The experimental group (n=4) received functionalized AuNS mixture (antiEGFR-pMBA-AuNS and antiPD-L1-DTNB-AuNS) and the control group (n=3) was pre-blocked with IP delivery of anti-EGFRa + anti-PD-L1a prior to AuNS injection. Differences in Au content between experimental and control groups was statistically significant for tumors retrieved at 6h post AuNS delivery ($p < 0.05$). Differences in Au content of tumors for the experimental group was also statistically significant ($p < 0.05$) between the maximum accumulation time (6 h) and at the end of the study (72 h).

We performed histochemical analysis of tumor sections to understand the biocompatibility of functionalized AuNS *in vivo*. Silver enhancement stains of tissue were performed which allows visualization of AuNS as gold selectively catalyzes the reduction of silver ions and deposits metallic silver which embeds the AuNS in kidney sections visible under a light microscope. The dark spots (Fig. 5a) in tumor sections from the experimental group indicate the presence of functionalized AuNS bound to the cell surface (Fig. 5a), not present in tumors without AuNS. Haematoxylin and Eosin (H&E) staining of the tumor sections both with and without functionalized AuNS was also performed to ensure the biocompatibility of AuNS (Fig. S7†). H&E identified that the cellular morphology of tumor tissues did not have any detrimental effect in the presence of AuNS indicating that they are nontoxic to cells.

Quantitative longitudinal analysis of biodistribution of nanoparticles in tissue after systemic delivery is necessary to evaluate their pharmacokinetics, uptake in tumor relative to other tissues, and their stability and potential toxicity *in vivo*. We studied the bioavailability and clearance of functionalized AuNS with inductively coupled plasma mass spectroscopy (IC-PMS) to measure the Au content in tumors and major organs at 6 h (maximum accumulation) and 72 h after IV delivery of AuNS (Fig. 5b). Acid digestion method was used to dissolve gold in the tissues into the solution for mass spectroscopy reading. At both 6 h and 72 h, very few gold was found in the stomach (2.8 ± 1.4), heart (5.2 ± 3.0) and lungs (4.0 ± 3.5). Minimal amounts of Au was found in the brain (0.5 ± 0.6) since the blood brain barrier does not allow entry of functionalized AuNS.^{56, 57} The majority of gold content was found in both mononuclear phagocyte system (MPS) organs at 72 h, spleen (724.6 ± 156.2) and liver (142.4 ± 60.9). There is significantly higher Au content in spleen at 72 h (724.6 ± 156.2) relative to 6 h (210.9 ± 88.3) which is statistically significant ($p < 0.05$), demonstrating AuNS mostly clear through the spleen.

Clearance of nanoparticles through MPS is not surprising and has been reported previously for other gold nanoparticles.⁵⁸⁻⁶¹ The presence of Au in kidneys (20.7 ± 6.7) was minimal since nanoparticles >10 nm are less likely to have renal clearance via glomerular filtration in mice.⁶²⁻⁶⁴ However, deviation to this trend has been observed previously where PEG coated Au nanoparticles were targeted to the mesangium of the kidney, the thin membrane of cells that supports glomerular capillaries, and accumulation in kidneys was observed for ~ 75 nm nanoparticles.⁶⁵ The nanoparticle morphology, including size, shape, and aspect ratio, has been shown to play a strong role in their clearance pathways, where anisotropic nanostructures with optimized aspect ratio have been shown to have renal clearance.⁶⁶⁻⁶⁸ Whereas clearance of AuNS through the MPS is expected in mice, this should not hinder clinical translation of AuNS as sub-micron and micron-sized particles have been shown to have renal clearance through the kidney in large animals and humans.^{69, 70} We also compared the Au content in tumors from the experimental group with the pre-blocked control tumors at maximum accumulation time-point (6 h post functionalized AuNS injection) and observed statistically significant differences in Au content ($p < 0.05$) (Fig. 5c). Moreover, significantly higher AuNS uptake was observed at the maximum accumulation time (6h) than at the end of the study (72h) for the experimental group ($p < 0.05$). The differences in AuNS content indicates the clearance of AuNS at the end of the study. The trends observed in IC-PMS correlate well with our *in vivo* endpoints where a significant difference in Raman signal was detected at 6h time-point and rapid decrease in signal was observed by 72h. Lastly, AuNS content in major organs were also compared between the experimental group with the pre-blocked control at the end of the study and no significant difference was found (Fig. S8†).

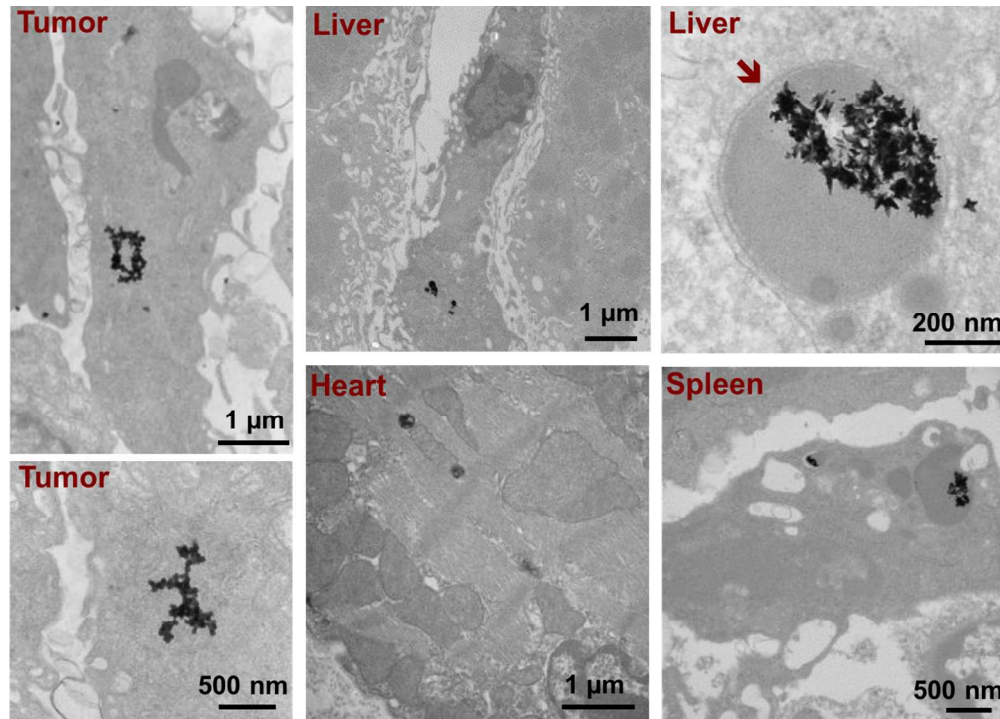


Figure 6. Transmission electron micrographs showing accumulation of functionalized AuNS in breast cancer tumors and major organs. The functionalized AuNS maintained their structural integrity after circulation in the body and were found in the tumor, in macrophages of the spleen, and in Kupffer cells of the liver via intracellular vesicles (indicated by the red arrow). Functionalized AuNS were not observed in the heart of the mouse.

Further, we obtained transmission electron microscopy (TEM) images of tumors and major organs to understand the internalization and localization of functionalized AuNS in the tumor microenvironment and in MPS of liver and spleen (Fig. 6). Tumor xenografts were retrieved at 6h post AuNS delivery *in vivo*, then fixed and sectioned for TEM imaging. Functionalized AuNS were observed in intracellular vesicles in the tumor but were not found in the mitochondria, the nucleus, or other cellular organelles. AuNS uptake and internalization in tumors is facilitated both by the EPR effect as well as receptor-mediated endocytosis enabled by targeting antibodies on the AuNS surface.^{39, 71-73} Liver and spleen were retrieved at the end of the study i.e. 72h time-point. Functionalized AuNS were found in the Kupffer cells of the liver and macrophages of the spleen. Nanoparticle uptake in Kupffer cells and macrophages have been

previously reported in the literature.⁷⁴⁻⁷⁸ In addition, AuNS were also found in lysosome-like structures within the macrophages, indicating endocytosis was the major mechanism for particle uptake. Lastly, we also retrieved the mouse hearts at the end of the study and did not find any AuNS which corroborates literature findings that gold nanoparticles cannot penetrate through the continuous endothelium cells in the arteries.⁷⁹⁻⁸¹ Notably, TEM images also clearly demonstrated that the functionalized AuNS maintained their structural and morphological integrity after IV delivery.

Conclusion

In summary, in this work we demonstrate the utility of AuNS labeled with Raman tags and antibodies to diagnose immunomarker PD-L1 and concurrently detect EGFR in MDA-MB-231 breast cancer tumors *in vivo* and *ex vivo* with noninvasive surface-enhanced Raman spectroscopy (SERS). Tracking of AuNS *in vivo* provide a longitudinal analysis of AuNS accumulation in tumors and simultaneous detection of PD-L1 and EGFR. Furthermore, SERS spatial maps of tumor sections *ex vivo* showed excellent correlation of AuNS distribution to vascular density, and enabled both qualitative and quantitative assessment of biomarker status in tumors. The bioavailability and clearance of AuNS was evaluated both with IC-PMS and TEM imaging which revealed AuNS accumulate in the tumors likely via receptor-mediated endocytosis and cleared by MPS. This study highlights the potential of SERS with dose-controlled AuNS to transform the diagnosis of cancer patients and enable patient-tailored immunotherapies. We anticipate that early monitoring with SERS will allow practitioners to determine the optimal treatment regimen of single checkpoint blockade or combination therapies to enable remission-free survival. Since PD-L1 and EGFR upregulation has been correlated to many cancers including non-small cell lung, renal, and colon cancer, multiplexed SERS with AuNS will also

benefit patients beyond breast cancer. The utility of SERS as both a powerful *in vivo* and *ex vivo* diagnostic tool will ultimately eliminate the need for unpredictable immunohistochemistry, and allow assessment of multiple immunomarkers within the same biopsy, minimizing repeated invasive procedures and patient discomfort. We expect this work will enable a path forward to clinically translate engineered gold nanostructures for both detection of immunomarkers and for therapeutic delivery of immunomodulators and vaccines.⁸²⁻⁸⁵

Conflicts of interests

The authors declare no competing financial interest.

Author Contributions

YO, JW and RB conceived the idea of the project and directed the project. YO and JW performed majority of the animal experiments. RB and YO wrote the manuscript. CO, IP and AM-J designed, and built the custom *in vivo* Raman spectroscopy instrument and wrote the code for data analysis. E. Lin contributed in *ex vivo* tumor Raman data analysis. EP, DC and SO assisted with animal welfare (weight and tumor size measurements etc), longitudinal Raman measurement (post-anesthesia care) and gold nanoantennas biodistribution experiments (organs retrieval). ML-L contributed in animal procedures training. EL helped with maintaining MDA-MB-231 cell line. RCD helped with ICPMS sample preparation, sample running, and data analysis

Acknowledgements

YO acknowledges support from American Cancer Society Institutional Research Grant (IRG-58-009-56), National Center for Advancing Translational Sciences CTSA award UL1TR000445, and CDMRP Peer reviewed Cancer research program grant CA171106. JAW acknowledges support from the National Science Foundation Graduate Research Fellowship Program under Grant Number 1445197. EP acknowledges support from National Science Foundation grant CMMI-1634856. CMO acknowledges NSF Graduate Research Fellowship. IJP acknowledges support from the National Institute of Health NRSA F31 Fellowship. RCD acknowledges supports from Vanderbilt's Trans Institutional Programs grant: Materials Durability and Environmental Research Facilities Hub (Faculty PIs - Florence Sanchez and David Kosson). TEM micrographs of AuNS were acquired with an instrument supported by NSF EPS 1004083. TEM images of tumor and organs were acquired by using VUMC Cell Imaging Shared Resource (supported by NIH grants CA68485, DK20593, DK58404, DK59637 and EY08126).

References

1. G. L. Beatty and W. L. Gladney, *Clin. Cancer Res.*, 2015, **21**, 687-692.
2. L. Chen and D. B. Flies, *Nat. Rev. Immunol.*, 2013, **13**, 227-242.
3. T. F. Gajewski, H. Schreiber and Y.-X. Fu, *Nat. Immunol.*, 2013, **14**, 1014-1022.
4. F. Bertucci and A. Goncalves, *Curr. Oncol. Rep.*, 2017, **19**, 64.
5. R. Iacovelli, F. Nole, E. Verri, G. Renne, C. Paglino, M. Santoni, M. Cossu Rocca, P. Giglione, G. Aurilio, D. Cullura, S. Cascinu and C. Porta, *Target Oncol.*, 2016, **11**, 143-148.
6. A. H. Scheel, S. Ansen, A. M. Schultheis, M. Scheffler, R. N. Fischer, S. Michels, M. Hellmich, J. George, T. Zander, M. Brockmann, E. Stoelben, H. Groen, W. Timens, S. Perner, M. von Bergwelt-Baildon, R. Buttner and J. Wolf, *Oncoimmunology*, 2016, **5**, e1131379.
7. J. C. Sunshine, P. L. Nguyen, G. J. Kaunitz, T. R. Cottrell, S. Berry, J. Esandrio, H. Xu, A. Ogurtsova, K. B. Bleich, T. C. Cornish, E. J. Lipson, R. A. Anders and J. M. Taube, *Clin. Cancer Res.*, 2017, **23**, 4938-4944.
8. D. M. Pardoll, *Nat. Rev. Cancer*, 2012, **12**, 252-264.
9. M. A. Postow, M. K. Callahan and J. D. Wolchok, *J. Clin. Oncol.*, 2015, **33**, 1974-1982.
10. H. Läubli, C. Balmelli, M. Bossard, O. Pfister, K. Glatz and A. Zippelius, *J. Immunother. Cancer*, 2015, **3**, 11.

11. A. A. Tarhini, H. Zahoor, J. H. Yearley, C. Gibson, Z. Rahman, R. Dubner, U. N. Rao, C. Sander and J. M. Kirkwood, *J. Transl. Med.*, 2015, **13**, 319.
12. L. P. Diggs and E. C. Hsueh, *Biomark. Res.*, 2017, **5**, 12.
13. R. Brody, Y. Zhang, M. Ballas, M. K. Siddiqui, P. Gupta, C. Barker, A. Midha and J. Walker, *Lung Cancer*, 2017, **112**, 200-215.
14. H. Ghebeh, C. Lehe, E. Barhoush, K. Al-Romaih, A. Tulbah, M. Al-Alwan, S.-F. Hendrayani, P. Manogaran, A. Alaiya, T. Al-Tweigeri, A. Aboussekhra and S. Dermime, *Breast Cancer Res.*, 2010, **12**, R48.
15. L. Deng, H. Liang, B. Burnette, M. Beckett, T. Darga, R. R. Weichselbaum and Y. X. Fu, *J. Clin. Invest.*, 2014, **124**, 687-695.
16. E. A. Mittendorf, A. V. Philips, F. Meric-Bernstam, N. Qiao, Y. Wu, S. Harrington, X. Su, Y. Wang, A. M. Gonzalez-Angulo, A. Akcakanat, A. Chawla, M. Curran, P. Hwu, P. Sharma, J. K. Litton, J. J. Molldrem and G. Alatrash, *Cancer Immunol. Res.*, 2014, **2**, 361-370.
17. H. Masuda, D. Zhang, C. Bartholomeusz, H. Doihara, G. N. Hortobagyi and N. T. Ueno, *Breast Cancer Res. Treat.*, 2012, **136**, 331-345.
18. Y. Tang, W. Fang, Y. Zhang, S. Hong, S. Kang, Y. Yan, N. Chen, J. Zhan, X. He and T. Qin, *Oncotarget*, 2015, **6**, 14209.
19. C. W. Li, S. O. Lim, W. Xia, H. H. Lee, L. C. Chan, C. W. Kuo, K. H. Khoo, S. S. Chang, J. H. Cha, T. Kim, J. L. Hsu, Y. Wu, J. M. Hsu, H. Yamaguchi, Q. Ding, Y. Wang, J. Yao, C. C. Lee, H. J. Wu, A. A. Sahin, J. P. Allison, D. Yu, G. N. Hortobagyi and M. C. Hung, *Nat. Commun.*, 2016, **7**, 12632.
20. N. Chen, W. Fang, J. Zhan, S. Hong, Y. Tang, S. Kang, Y. Zhang, X. He, T. Zhou, T. Qin, Y. Huang, X. Yi and L. Zhang, *J. Thorac. Oncol.*, 2015, **10**, 910-923.
21. L. A. Lane, X. Qian and S. Nie, *Chem. Rev.*, 2015, **115**, 10489-10529.
22. A. Pallaoro, M. R. Hoonejani, G. B. Braun, C. D. Meinhart and M. Moskovits, *ACS Nano*, 2015, **9**, 4328-4336.
23. L. Tian, J. J. Morrissey, R. Kattumenu, N. Gandra, E. D. Kharasch and S. Singamaneni, *Anal. Chem.*, 2012, **84**, 9928-9934.
24. K. K. Maiti, U. S. Dinish, A. Samanta, M. Vendrell, K.-S. Soh, S.-J. Park, M. Olivo and Y.-T. Chang, *Nano Today*, 2012, **7**, 85-93.
25. C. L. Zavaleta, B. R. Smith, I. Walton, W. Doering, G. Davis, B. Shojaei, M. J. Natan and S. S. Gambhir, *Proc. Natl. Acad. Sci.*, 2009, **106**, 13511-13516.
26. U. S. Dinish, G. Balasundaram, Y. T. Chang and M. Olivo, *Sci. Rep.*, 2014, **4**, 4075.
27. M. F. Kircher, A. de la Zerda, J. V. Jokerst, C. L. Zavaleta, P. J. Kempen, E. Mittra, K. Pitter, R. Huang, C. Campos, F. Habte, R. Sinclair, C. W. Brennan, I. K. Mellinghoff, E. C. Holland and S. S. Gambhir, *Nat. Med.*, 2012, **18**, 829-834.
28. M. Jermyn, K. Mok, J. Mercier, J. Desroches, J. Pichette, K. Saint-Arnaud, L. Bernstein, M.-C. Guiot, K. Petrecca and F. Leblond, *Sci. Transl. Med.*, 2015, **7**, 274ra219-274ra219.
29. J. Q. Nguyen, Z. S. Gowani, M. O'Connor, I. J. Pence, T. Q. Nguyen, G. E. Holt, H. S. Schwartz, J. L. Halpern and A. Mahadevan-Jansen, *Lasers Surg. Med.*, 2016, **48**, 774-781.
30. H. Kang, S. Jeong, Y. Park, J. Yim, B.-H. Jun, S. Kyeong, J.-K. Yang, G. Kim, S. Hong, L. P. Lee, J.-H. Kim, H.-Y. Lee, D. H. Jeong and Y.-S. Lee, *Adv. Funct. Mater.*, 2013, **23**, 3719-3727.
31. G. von Maltzahn, A. Centrone, J. H. Park, R. Ramanathan, M. J. Sailor, T. A. Hatton and S. N. Bhatia, *Adv. Mater.*, 2009, **21**, 3175-3180.

32. J. A. Webb, W. R. Erwin, H. F. Zarick, J. Aufrecht, H. W. Manning, M. J. Lang, C. L. Pint and R. Bardhan, *J. Phys. Chem. C*, 2014, **118**, 3696-3707.
33. P. A. Gorry, *Anal. Chem.*, 1990, **62**, 570-573.
34. J. Luo, K. Ying and J. Bai, *Signal Process.*, 2005, **85**, 1429-1434.
35. A. Savitzky and M. J. E. Golay, *Anal. Chem.*, 1964, **36**, 1627-1639.
36. C. A. Lieber and A. Mahadevan-Jansen, *Appl. Spectrosc.*, 2003, **57**, 1363-1367.
37. Y. C. Ou, J. A. Webb, S. Faley, D. Shae, E. M. Talbert, S. Lin, C. C. Cutright, J. T. Wilson, L. M. Bellan and R. Bardhan, *ACS Omega*, 2016, **1**, 234-243.
38. J. A. Webb, Y. C. Ou, S. Faley, E. P. Paul, J. P. Hittinger, C. C. Cutright, E. C. Lin, L. M. Bellan and R. Bardhan, *ACS Omega*, 2017, **2**, 3583-3594.
39. R. A. Petros and J. M. DeSimone, *Nat. Rev. Drug Discov.*, 2010, **9**, 615-627.
40. S. Mitra, U. Gaur, P. Ghosh and A. Maitra, *J. Control. Release*, 2001, **74**, 317-323.
41. Y. Wang, L. Polavarapu and L. M. Liz-Marzán, *ACS Appl. Mater. Interfaces*, 2014, **6**, 21798-21805.
42. J. A. Webb, J. Aufrecht, C. Hungerford and R. Bardhan, *J. Mater. Chem. C*, 2014, **2**, 10446-10454.
43. J. A. Webb and R. Bardhan, *Nanoscale*, 2014, **6**, 2502-2530.
44. P. Xu, S.-H. Jeon, N. H. Mack, S. K. Doorn, D. J. Williams, X. Han and H.-L. Wang, *Nanoscale*, 2010, **2**, 1436-1440.
45. C. Wang, J. Xu, J. Wang, Z. Rong, P. Li, R. Xiao and S. Wang, *J. Mater. Chem. C*, 2015, **3**, 8684-8693.
46. Y. Liu, J. R. Ashton, E. J. Moding, H. Yuan, J. K. Register, A. M. Fales, J. Choi, M. J. Whitley, X. Zhao, Y. Qi, Y. Ma, G. Vaidyanathan, M. R. Zalutsky, D. G. Kirsch, C. T. Badea and T. Vo-Dinh, *Theranostics*, 2015, **5**, 946-960.
47. C. M. O'Brien, J. L. Herington, N. Brown, I. J. Pence, B. C. Paria, J. C. Slaughter, J. Reese and A. Mahadevan-Jansen, *Sci. Rep.*, 2017, **7**, 6835.
48. I. J. Pence, D. B. Beaulieu, S. N. Horst, X. Bi, A. J. Herline, D. A. Schwartz and A. Mahadevan-Jansen, *Biomed. Opt. Express*, 2017, **8**, 524-535.
49. R. Bardhan, W. Chen, M. Bartels, C. Perez-Torres, M. F. Botero, R. W. McAninch, A. Contreras, R. Schiff, R. G. Pautler, N. J. Halas and A. Joshi, *Nano Lett.*, 2010, **10**, 4920-4928.
50. W. Chen, C. Ayala-Orozco, N. C. Biswal, C. Perez-Torres, M. Bartels, R. Bardhan, G. Stinnet, X.-D. Liu, B. Ji and A. Deorukhkar, *Nanomedicine*, 2014, **9**, 1209-1222.
51. S. Heskamp, W. Hobo, J. D. Molkenboer-Kuennen, D. Olive, W. J. Oyen, H. Dolstra and O. C. Boerman, *Cancer Res.*, 2015, **75**, 2928-2936.
52. R. Tavare, H. Escuin-Ordinas, S. Mok, M. N. McCracken, K. A. Zettlitz, F. B. Salazar, O. N. Witte, A. Ribas and A. M. Wu, *Cancer Res.*, 2016, **76**, 73-82.
53. H. Kobayashi, R. Watanabe and P. L. Choyke, *Theranostics*, 2013, **4**, 81-89.
54. L. Miao and L. Huang, in *Nanotechnology-Based Precision Tools for the Detection and Treatment of Cancer*, eds. C. A. Mirkin, T. J. Meade, S. H. Petrosko and A. H. Stegh, Springer International Publishing, Cham, 2015, DOI: 10.1007/978-3-319-16555-4_9, pp. 193-226.
55. C. G. England, A. M. Gobin and H. B. Frieboes, *Eur. Phys. J. Plus*, 2015, **130**.
56. N. Khlebtsov and L. Dykman, *Chem. Soc. Rev.*, 2011, **40**, 1647-1671.
57. G. Sonavane, K. Tomoda and K. Makino, *Colloids Surf. B Biointerfaces*, 2008, **66**, 274-280.

58. W. H. De Jong, W. I. Hagens, P. Krystek, M. C. Burger, A. J. Sips and R. E. Geertsma, *Biomaterials*, 2008, **29**, 1912-1919.
59. H. H. Gustafson, D. Holt-Casper, D. W. Grainger and H. Ghandehari, *Nano Today*, 2015, **10**, 487-510.
60. E. Blanco, H. Shen and M. Ferrari, *Nat. Biotechnol.*, 2015, **33**, 941-951.
61. N. Oh and J.-H. Park, *ACS Nano*, 2014, **8**, 6232-6241.
62. J. Liu, M. Yu, C. Zhou and J. Zheng, *Mater. Today*, 2013, **16**, 477-486.
63. H. S. Choi, W. Liu, P. Misra, E. Tanaka, J. P. Zimmer, B. Itty Ipe, M. G. Bawendi and J. V. Frangioni, *Nat. Biotechnol.*, 2007, **25**, 1165-1170.
64. M. E. Davis, Z. G. Chen and D. M. Shin, *Nat. Rev. Drug Discov.*, 2008, **7**, 771-782.
65. C. H. J. Choi, J. E. Zuckerman, P. Webster and M. E. Davis, *Proc. Natl. Acad. Sci.*, 2011, **108**, 6656-6661.
66. X. Huang, L. Li, T. Liu, N. Hao, H. Liu, D. Chen and F. Tang, *ACS Nano*, 2011, **5**, 5390-5399.
67. R. Toy, P. M. Peiris, K. B. Ghaghada and E. Karathanasis, *Nanomedicine*, 2014, **9**, 121-134.
68. Arnida, M. M. Janat-Amsbury, A. Ray, C. M. Peterson and H. Ghandehari, *Eur. J. Pharm. Biopharm.*, 2011, **77**, 417-423.
69. S. Wiegand, T. Heinen, A. Ramaswamy, A. M. Sesterhenn, C. Bergemann, J. A. Werner and A. S. Lubbe, *J. Drug Target.*, 2009, **17**, 194-199.
70. A. M. Gatti and F. Rivasi, *Biomaterials*, 2002, **23**, 2381-2387.
71. B. Kang, A. Kukreja, D. Song, Y.-M. Huh and S. Haam, *J. Bio. Eng.*, 2017, **11(13)**, 1-12.
72. J. Rejman, V. Oberle, I. S. Zuhorn and D. Hoekstra, *Biochem. J.*, 2004, **377**, 159-169.
73. A. Z. Wang, R. Langer and O. C. Farokhzad, *Annu. Rev. Med.*, 2012, **63**, 185-198.
74. E. Sadauskas, H. Wallin, M. Stoltenberg, U. Vogel, P. Doering, A. Larsen and G. Danscher, *Part. Fibre. Toxicol.*, 2007, **4**, 10.
75. W. H. D. Jong, M. C. Burger, M. A. Verheijen and R. E. Geertsma, *Materials*, 2010, **3**, 4681-4694.
76. S. A. MacParland, K. M. Tsoi, B. Ouyang, X.-Z. Ma, J. Manuel, A. Fawaz, M. A. Ostrowski, B. A. Alman, A. Zilman, W. C. W. Chan and I. D. McGilvray, *ACS Nano*, 2017, **11**, 2428-2443.
77. K. M. Tsoi, S. A. MacParland, X. Z. Ma, V. N. Spetzler, J. Echeverri, B. Ouyang, S. M. Fadel, E. A. Sykes, N. Goldaracena, J. M. Kathis, J. B. Conneely, B. A. Alman, M. Selzner, M. A. Ostrowski, O. A. Adeyi, A. Zilman, I. D. McGilvray and W. C. Chan, *Nat. Mater.*, 2016, **15**, 1212-1221.
78. L. A. Dykman and N. G. Khlebtsov, *Chem. Sci.*, 2017, **8**, 1719-1735.
79. S. Huo, H. Ma, K. Huang, J. Liu, T. Wei, S. Jin, J. Zhang, S. He and X. J. Liang, *Cancer Res.*, 2013, **73**, 319-330.
80. C. Yang, A. Tian and Z. Li, *Sci. Rep.*, 2016, **6**, 20203.
81. S. Barua and S. Mitragotri, *Nano Today*, 2014, **9**, 223-243.
82. R. Meir, K. Shamalov, O. Betzer, M. Motiei, M. Horovitz-Fried, R. Yehuda, A. Popovtzer, R. Popovtzer and C. J. Cohen, *ACS Nano*, 2015, **9**, 6363-6372.
83. P. Zhang, Y.-C. Chiu, L. H. Tostanoski and C. M. Jewell, *ACS Nano*, 2015, **9**, 6465-6477.
84. Y. Liu, P. Maccarini, G. M. Palmer, W. Etienne, Y. Zhao, C. T. Lee, X. Ma, B. A. Inman and T. Vo-Dinh, *Sci. Rep.*, 2017, **7**, 8606.

85. R. Meir, K. Shamalov, T. Sadan, M. Motiei, G. Yaari, C. J. Cohen and R. Popovtzer, *ACS Nano*, 2017, DOI: 10.1021/acsnano.7b05299.